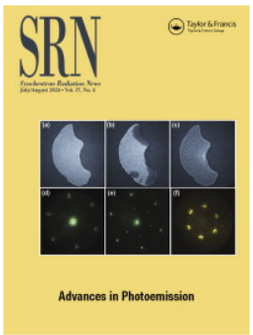

Synchrotron Radiation News

ISSN: (Print) (Online) Journal homepage: www.tandfonline.com/journals/gsrn20

Exploring Spin- and Momentum-Resolved Phenomena at the NanoESCA Beamline of Elettra Synchrotron

Giovanni Zamborlini, Matteo Jugovac, Iulia Cojocariu, Daniel Baranowski, Simone Mearini, Yan Yan Grisan Qiu, Vitaliy Feyer & Claus Michael Schneider

To cite this article: Giovanni Zamborlini, Matteo Jugovac, Iulia Cojocariu, Daniel Baranowski, Simone Mearini, Yan Yan Grisan Qiu, Vitaliy Feyer & Claus Michael Schneider (2024) Exploring Spin- and Momentum-Resolved Phenomena at the NanoESCA Beamline of Elettra Synchrotron, Synchrotron Radiation News, 37:4, 24-29, DOI: 10.1080/08940886.2024.2391253

To link to this article: https://doi.org/10.1080/08940886.2024.2391253

Published online: 28 Aug 2024.

TECHNICAL REPORT OPEN ACCESS

Exploring Spin- and Momentum-Resolved Phenomena at the NanoESCA Beamline of Elettra Synchrotron

Giovanni Zamborlini,[1,2] Matteo Jugovac,[1,3] Iulia Cojocariu,[1,4] Daniel Baranowski,[1] Simone Mearini,[1] Yan Yan Grisan Qiu,[1] Vitaliy Feyer,[1] and Claus Michael Schneider[1,5,6]

[1]*Peter Grünberg Institute (PGI-6), Jülich Research Centre, Jülich, Germany*
[2]*Institute of Physics, University of Graz, Graz, Austria*
[3]*Elettra-Sincrotrone Trieste S.C.p.A, Trieste, Italy*
[4]*Physics Department, University of Trieste, Trieste, Italy*
[5]*Faculty of Physics and Center for Nanointegration Duisburg-Essen (CENIDE), University of Duisburg-Essen, Duisburg, Germany*
[6]*Department of Physics and Astronomy, UC Davis, Davis, CA, USA* v.feyer@fz-juelich.de

Magnetism in solids is a complex phenomenon that arises from the intrinsic magnetic properties of electrons within the material. These intrinsic properties include the "spin" of the electrons—a quantum mechanical property—and various spin-dependent interactions. In materials with magnetic ordering, such as ferromagnetic or antiferromagnetic materials, the magnetic moments of individual atoms or ions align cooperatively, resulting in a specific macroscopic magnetic behavior. One of the key factors influencing the magnetism in solids is the spin polarization of electrons, where the quantity spin polarization refers to the preferential alignment of electron spins in a particular direction within a material. This alignment can be influenced by various factors, including, for example, the crystal structure, the presence of magnetic impurities or dopants, spin-orbit coupling, and external magnetic fields [1].

In itinerant magnetism, which is commonly observed in materials such as 3*d* transition metals, the magnetic behavior arises from the collective motion of electrons throughout the material. In these materials, electrons with different spin orientations may exhibit different energy levels and densities of states, leading to a variety of spin-dependent effects in the electronic structure [2].

One consequence of spin-polarized electronic states is the Rashba effect, a peculiar phenomenon arising from the combination of spin-orbit coupling with an asymmetry of the crystal potential in nonmagnetic materials. The latter occurs predominantly by breaking the inversion symmetry of the potential at a surface or an interface in the crystal. This effect finds its origin in the interaction between the electron's spin $\vec{S}$ and its motion within the crystal lattice, described by the momentum vector $\vec{k}$. As a result, we find (a) a splitting of energy bands, (b) the emergence of spin-polarized surface states, and (c) a "spin-momentum locking", i.e., a coupling of the spin $\vec{S}$ and the local momentum $\vec{k}$ [3]. The Rashba effect is of particular interest in spintronics and semiconductor physics, as it can be exploited to manipulate electron spins for various applications, such as spin-based electronic devices and quantum computing.

Overall, the magnetism in solids arises from a complex interplay of electronic and spin-dependent interactions, crystal structure, and external influences, making it a rich area of study in condensed matter physics and materials science. In many cases, it is important not only to characterize the energy distribution of electrons in the solid, but also to obtain information about its spin properties. In this respect, spin-resolved photoemission spectroscopy is a powerful and well-established tool for probing spin-dependent electronic structures, which, coupled with appropriate theoretical models, offers insights into band structure, exchange interactions, and spin-orbit effects [4].

On the one hand, technological development also has an impact on the characterization and analysis approaches. As devices in modern technology shrink to sub-micrometer scales, precise control over interfaces and structures paired with high lateral resolution becomes crucial. In this context, the photoelectron emission microscope (PEEM) emerges as a vital tool for high-resolution imaging, enabling the investigation of physical and chemical properties with enhanced lateral resolution [5]. On the other hand, an energy-filtered PEEM can also be operated in the momentum space mode [6–8]. In this so-called momentum microscopy mode operation, an additional Fourier lens in the objective column converts the real space image into a momentum distribution image. The momentum microscope family comprises several types of instruments, including the energy-dispersive type employing either a tandem arrangement of two hemispherical analyzers [6–8] or a single hemispherical analyzer [9–11]. The key feature of all momentum microscopes is their large solid-angle acceptance, exploiting the full-field-imaging properties of the cathode lens. More recently, the integration of the momentum microscope concept with time-of-flight detection has resulted in the development of the ToF-momentum microscope [12].

The operational concept of a momentum microscope relies on a fundamental optical principle whereby the backfocal plane of an objective lens contains a reciprocal image, known as a Fourier image in mathematical terms [5–8]. Momentum microscopes capture extensive intervals in the (E_{kin}, k_x, k_y) parameter space without requiring sample rotation or angular scanning. This allows for obtaining energy and momentum-dependent cuts of the surface Brillouin zone of the material

under investigation. However, it is important to note that the momentum-resolved images may not directly reflect the electronic ground state structure, as selection rules and cross sections must be considered in the photoemission process.

The PEEM installed at the NanoESCA beamline at Elettra synchrotron contains an electron-optical column with an objective lens capable of operating at up to +30 kV acceleration voltage, leaving the sample close to ground potential. This prototype system has been specifically designed for its use with synchrotron radiation. The NanoESCA end-station is operated by the Peter Grünberg Institute of Forschungszentrum Jülich [8]. Part of the soft X-ray beamline and the end-station are shown in Figure 1. The beamline has two undulator sources and a varied-line spacing (VLS) grating monochromator [13, 14]. The APPLE-2 type undulators can provide linear horizontal/vertical and circularly polarized X-rays from 25 eV up to 1300 eV [13]. The monochromator hosts two VLS gratings with 400 lines/mm and 200 lines/mm for higher and lower photon energies, respectively [13, 14]. The monochromatized photon flux on the sample is in the range $10^{12} - 10^{13}$ photons/s, depending on the photon energy and the dimension of the slits used, whereas the maximum photon flux is obtained at about 150 eV. The two elliptical refocusing mirrors in the Kirkpatrick-Baez configuration provide a focal spot on the sample both in the horizontal and vertical directions [13]. The X-ray beam size is measured to be about 10 µm × 6 µm (hor × ver). Considering that the beam is incident on the sample at 25° from the surface plane in the horizontal direction, the beam footprint on the sample is about 10 µm × 15 µm at best [8]. This geometry has been chosen to achieve a more homogeneously illuminated field-of-view (FoV) when used with synchrotron radiation. Apart from the adjustable bending of the mirrors used for optimizing the focus, the pitch of the two mirrors is used for precise positioning of the X-ray beam on the sample.

After the photoexcitation process, the emitted photoelectrons are accelerated toward the objective lens of the microscope (see Figure 1(b)). Upon entering the NanoESCA column, the electrons are decelerated to the column energy, which ranges between 1 and 2 keV depending on the acceleration voltage and objective lens settings. Subsequently, they are further retarded to the pass energy (E_{pass}) of the energy filter before entering the double-hemispherical analyzer. Projective lenses located after the energy filter magnify the image onto a detector consisting of a channel plate and fluorescent screen, usually captured by a Peltier-cooled slow-scan CCD camera (pco.1600 from PCO AG, Kelheim, Germany).

As already mentioned above, the PEEM instrument is equipped with a transfer lens after the exit slit (see Figure 1(b)). This lens enables the projection of the momentum distribution of the photoelectrons from the backfocal plane of the objective lens through an energy filter onto the image detector, resulting in a reciprocal or momentum map of the photoelectrons for a selected kinetic energy. The area on the sample surface from which this information originates can be defined by a field-limiting (selected area) aperture between the transfer lens and the projection/retardation optics. Thus, by combining real space and momentum imaging modes with easy switching between the two, we can correlate later-

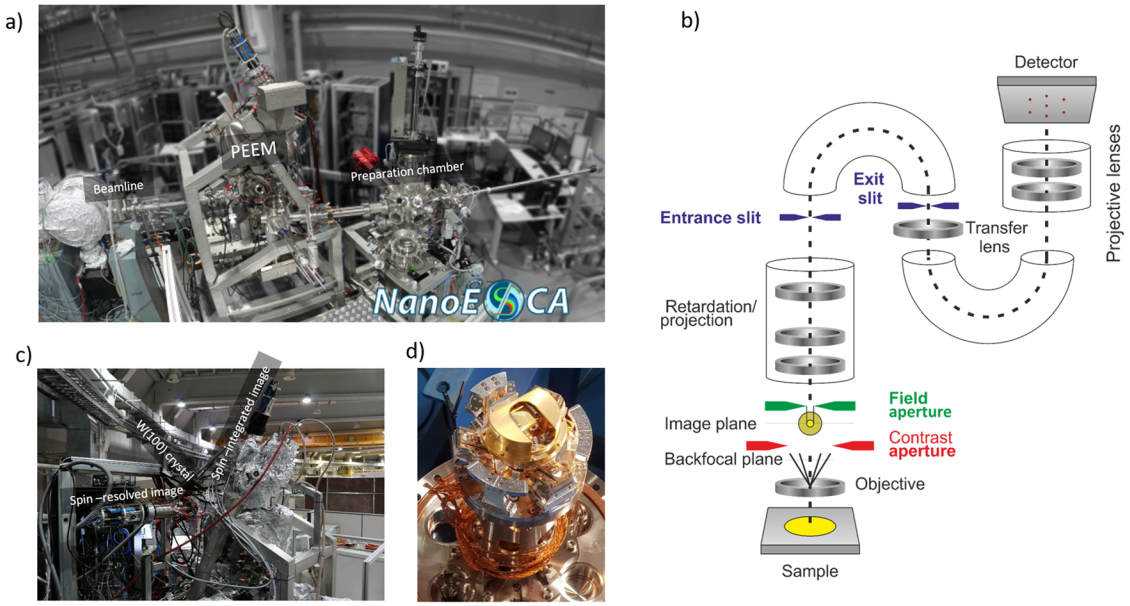

Figure 1: (a) The NanoESCA end-station installed at the beamline of the Elettra synchrotron radiation facility in Trieste (Italy). The synchrotron light enters through the beamline on the left-hand side. (b) Scheme illustrating the working principle of NanoESCA PEEM. (c) Projective columns for both spin-integrated and spin-resolved measurements, and the tungsten (W(100)) target for spin-resolved measurements. (d) The liquid helium-cooled sample manipulator with six degrees of freedom, temperature range: down to 30 K using liquid helium and 80 K with liquid nitrogen. The manipulator can be heated up to 400 K by means of a cartridge heater mounted on the cryostat.

ally resolved chemical and electronic information from a well-defined region on the sample surface.

The NanoESCA end-station is set up for experiments at cryogenic temperature (see Figure 1(d)). The sample manipulator has six degrees of freedom allowed by a SMARPOD motion system (SmarAct GmbH). The sample cooling is achieved by an open-cycle cryostat (Janis ST-400). The temperature is measured by a silicon diode (Lakeshore DT-670E-BR) at the sample holder and adjusted by changing the flow rate of liquid He or nitrogen. The minimum temperature of 30 K can be achieved using liquid He.

Advancements in spin detector technology have significantly improved the feasibility and accuracy of spin-resolved measurements, even for systems with inherently low count rates, such as topological insulators [15–17]. For example, multichannel spin filters, utilizing the specular reflection of electrons in the {00}-LEED beam on the surface of a single crystal, have opened up new opportunities for the utilization of this spin detector in conjunction with PEEM and time-of-flight instruments [7, 12]. The PEEM instrument at Elettra offers an option for spin-resolved measurements multichannel spin polarimeter based on {00}-LEED from a W(100) single crystal [18]. In particular, the experimental setup utilizes a W(100) single crystal, with the [001] direction aligned to the scattering plane at the exit optics of the NanoESCA microscope. This crystal is placed into the electron optical path immediately after the energy filter (see Figure 2(b), W(100) crystal, and spin-resolved image). The electrons entering the spin optics are decelerated from the pass energy to lower scattering energies (15–50 eV) before reaching the W target. The incident angle of the electron beam on the W target is set to 45 degrees, with the spin quantization axis being (P) normal to the scattering plane [19]. The image information is preserved upon 90-degree specular reflection and projected onto a dedicated 2D detector, consisting of a channel plate and fluorescent screen. The momentum images are captured by a Peltier-cooled slow-scan CCD camera (pco.1600 from PCO AG, Kelheim, Germany). The reflectivity of such a crystal has been estimated to be 0.012, effectively reducing the signal in a spin-resolved image by a factor of ~99 compared to a spin-integrated image [19].

The reflectivity curve of the W(100) is a critical parameter for assessing the quality of spin-resolved experiments. In particular, two scattering energies (26.5 and 30.5 eV) correspond to local maxima in the electron reflectivity having similar intensity [19]. Notably, the highest asymmetry in the spin-dependent electron reflection is observed when comparing these two energies. Therefore, by acquiring two images at these scattering energies, it becomes possible to discriminate the spin of the electrons, either in a real space image (depicting magnetic domains)

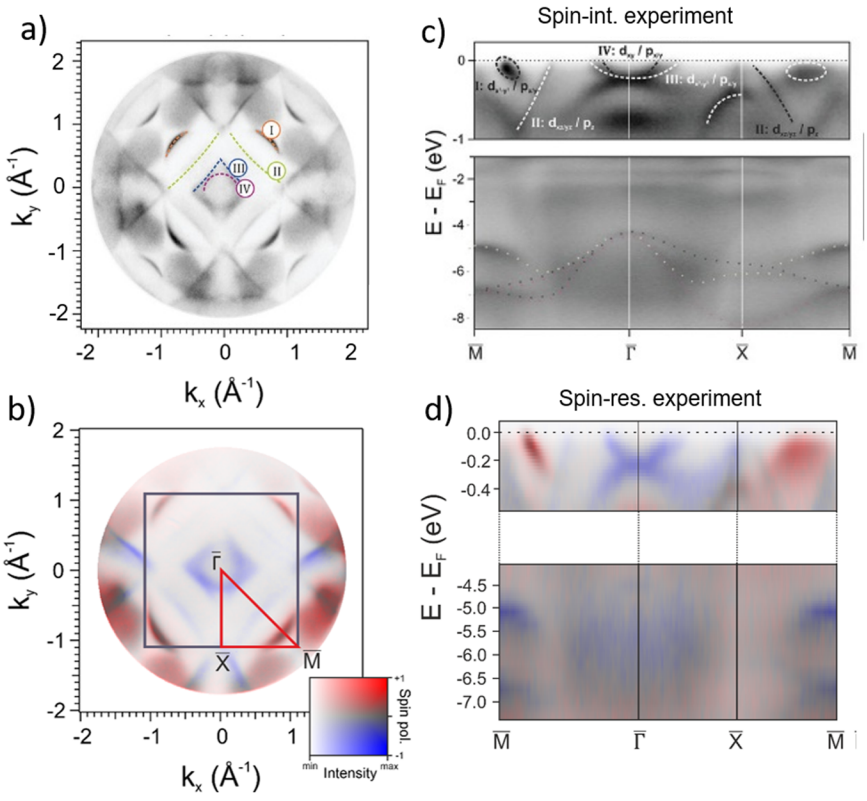

Figure 2: (a) Spin-integrated and (b) spin-resolved momentum map of the Fe(100)-p(1x1)O surface at the Fermi energy [22]. The surface First Brillouin Zone is highlighted by a violet square and the high symmetry points are connected by red lines. Experimentally obtained spin-integrated (c) and spin-resolved (d) band structure of Fe(100)-p(1x1)O.

or a reciprocal space image (revealing the spin-resolved electronic structure) [18]. To maximize the spin detection efficiency, the features under examination should have their spin lying in-plane and aligned with the optical axis of the microscope, as the spin filter is sensitive only to the projection of the spin along that axis.

The investigation of ferromagnetic (FM) samples offers a straightforward approach to test the applicability of spin-resolved measurements using the NanoESCA setup. In this scenario, the spin polarization of the photo-emitted electrons is determined by measuring two remnant magnetization states with opposite magnetization directions [20–22]. In a sample with a magnetic domain structure, this is most easily achieved by comparing the signals from neighboring domains.

The adsorption of non-magnetic atoms and molecules on an FM transition metal surface creates a hybrid interface exhibiting a plethora of novel exotic physical phenomena. For example, the adsorption of atomic oxygen atop ferromagnetic iron alters the electronic correlation and, thereby, affects the interfacial electronic and magnetic structure [22]. In particular, oxygen passivation of Fe(100) results in the formation of a Fe(100)-$p(1\times1)$O superstructure, causing the disappearance of the iron surface state [23], while introducing new electronic states. In the vicinity of the Fermi level (E_F), we observe four extrinsic surface states, denoted as I, II, III, and IV, with states III and IV being prominent across all photon energies near the $\bar{\Gamma}$ point (see Figure 2(a)). State I is evident near the $\bar{M}$ point, particularly at 64 eV, while state II exhibits little intensity at 40 eV due to photoionization cross-section considerations. Notably, all these states appear much sharper and more prominent than the ones for the clean Fe(100) surface [21, 22]. The observation can be directly related to the dramatic narrowing of the d-bands located close to the Fermi level caused by the larger electron correlation [22]. These phenomena become more evident when observing the energy dispersion of the highlighted features along the symmetry directions indicated in Figure 2(b). The resulting plot is depicted in Figure 2(c), where also the electronic orbital nature of the states associated with the Fe(100)-$p(1\times1)$O surface is emphasized. Their surface nature was confirmed by comparing photoemission measurements obtained at different photon energies, further supported by density functional theory (DFT) calculations that include dynamic mean field theory (DMFT) corrections. The states near the Fermi level are predominantly antibonding states formed between the antibonding O *p*- and the Fe *d* orbitals. Unlike the bonding states at –6 eV, their primary contribution arises from the Fe *d*-orbitals. Consequently, they are quasiparticle states, resembling single-particle electronic states, but renormalized by interaction effects. These states extend over a narrow energy range of approximately 1 eV width, and their flatter energy dispersion compared to the quasiparticle states of clean Fe is a consequence of the enhanced correlation effects, as mentioned above. The three parabolic dispersing states along the $\bar{X}-\bar{M}$-path at –6 eV originate from the bonding states between the 2*p* (p_x, p_y, p_z) orbitals of the oxygen and the *d* orbitals of the metal (see Figure 2(c)).

After assigning the main features of the surface band structure of the Fe(100)-p(1 × 1)O surface, the spin-resolved photoemission experiment was performed. It allows us to track the dispersion of the antibonding and bonding states in the two spin channels. To visualize both the intensity and the spin polarization within the same plot, the color scale is represented by a 2D map, as depicted in Figure 2(b,d). From these data, we can immediately extrapolate the spin character of the antibonding states near the Fermi level reported earlier. While the states close to the center of the surface Brillouin zone primarily originate from minority electrons (blue), the one located near the $\bar{M}$-point exhibits a strong majority character (red).

Based on these findings, it is suggested that the adsorption of atoms or small molecules enables the formation of intermediate correlated metallic regimes, which may not be observed in other materials. Moreover, well-established concepts developed to understand the physics and chemistry of adsorbate—FM metal interfaces, such as the *d*-band model [24, 25], need to be reevaluated with a strong focus on many-particle effects [22].

In the rapidly evolving landscape of electronic materials and devices, the integration of two-dimensional materials, particularly graphene, with magnetic elements has emerged as a promising frontier. In this context, the achievement of topological electronic flat bands near or at the Fermi level holds significant promise for the emergence of exotic electronic and magnetic states. One of the key attributes of flat bands is their easy electrical tunability, allowing for the exploration of correlated phases such as unconventional superconductivity, quantum states, and insulating topological states, all within two-dimensional platforms and without the requirement for an applied magnetic field.

An alternative method for generating flat bands in graphene involves exploiting the Spin-Orbit Coupling (SOC) effect induced by the proximity to magnetic and/or heavy-metal layers. Monolayer graphene (Gr) interfaced with 3*d*-ferromagnetic and 4*f*-materials presents compelling technological prospects, bridging the fields of spintronics, ultrafast graphene-based electronics, and photonics. While Gr/3*d*-ferromagnetic systems exhibit strong hybridization [26, 27] influencing the electronic properties of graphene, Gr/4*f*-ferromagnetic interfaces demonstrate a weaker interaction that preserves the electronic structure of the graphene layer [28].

In order to realize such a system, graphene is grown on a 10-nanometer-thick cobalt film via ethylene chemical vapor deposition (CVD), following a well-established recipe [26, 27]. The corresponding 2D momentum map acquired at the Fermi level and the system's band structure at the $\bar{K}$ point of the pristine Gr/Co interface are reported in Figure 3(a,c). As mentioned above, the strong interaction between graphene and cobalt leads to an orbital hybridization at the interface. Consequently, this leads to a shift to higher binding energy of the Dirac cone compared to freestanding graphene and the emergence of a hybrid state characterized by a single spin polarization, as previously shown using the NanoESCA end-station [26, 27].

Subsequently, metallic europium was deposited on top of Gr/Co and intercalated at the interface via thermal annealing. Eu arranges in a $\sqrt{3}x\sqrt{3}R30°$ structure, as confirmed by the reported low energy electron diffraction (LEED) experiment [28]. The presence of europium leads to

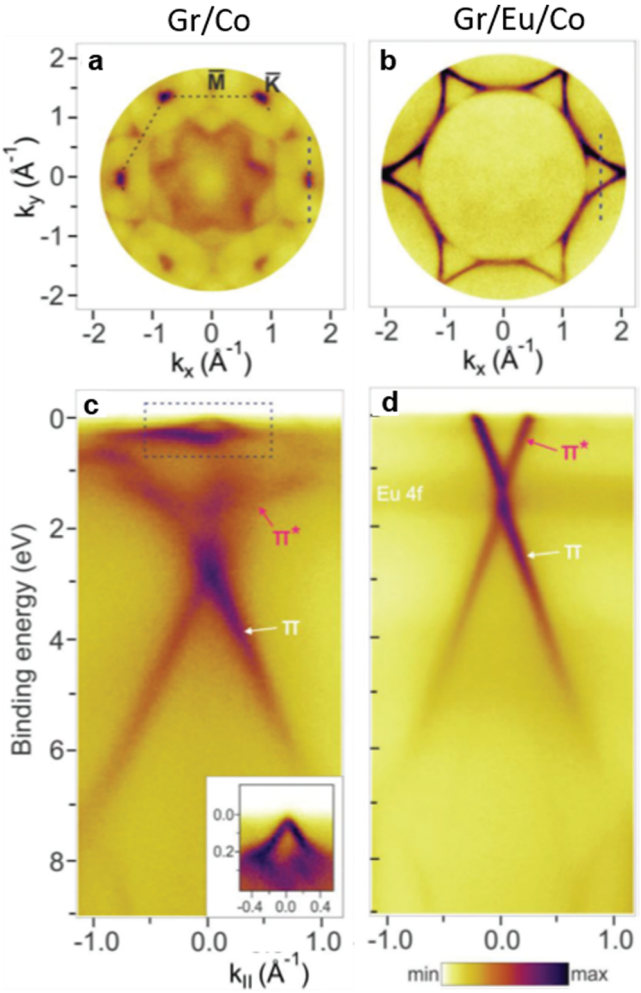

Figure 3: Spin-integrated momentum maps of the Gr/Co(0001) [28] (a) and Gr/Co(0001)/Gr at the Fermi energy. Band structure of Gr/Co(0001) (c) and Gr/Co(0001)/Gr (d) acquired at the $\bar{K}$ point of the first Brillouin zone for Gr/Co and Gr/Eu/Co, respectively.

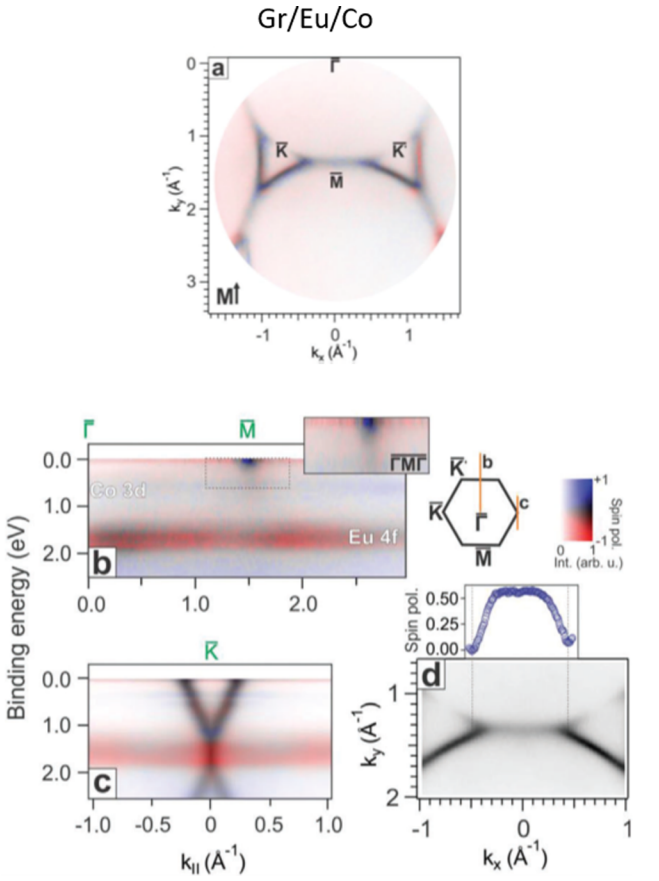

Figure 4: Spin-resolved electronic structure of the Eu/Gr/Co system [28]. (a) Spin-resolved 2D momentum maps at the Fermi level of the Eu/Gr/Co interface. Spin-resolved energy vs. momentum map acquired along the $\bar{\Gamma}-\bar{K}$ direction (b) and at the $\bar{K}$ point (c). (d) Spin-resolved momentum distribution curves acquired along the $\bar{\Gamma}-\bar{K}$ direction at the Fermi level (between 0.0 and 0.2 eV and marked by a solid black line at the right side of b)). (e) Spin polarization curve obtained by a normalized difference of the two curves in (d). According to the 2D color code on the right side of panel c), blue and red intensities correspond to majority and minority electronic states.

the decoupling of the graphene layer from the metallic support and, in parallel, to the doping via charge transfer from Eu to Gr. The doping level is sufficient to occupy the graphene π* band up to the van Hove singularity, leading to the observation of the flat band at the $\bar{M}$ point of the surface Brillouin zone (Figure 3(b,d)). Moreover, the SOC at the interface is responsible for the opening of a sizable band gap of 0.36 eV at the Dirac point (Figure 3(d)).

The spin character of the electronic bands near the Fermi level was probed using spin-resolved momentum microscopy at the NanoESCA beamline. In order to better visualize the flat band, the sample was tilted to be able to accept the $\bar{K}$, $\bar{M}$ and $\bar{K}'$ points in the 2D momentum map. The 2D spin-resolved momentum map at the Fermi level, reported in Figure 4(a), allows us to clearly visualize the shape and polarization of the π* states, which are occupied due to electron transfer from Eu. It can be appreciated that the electron pockets formed by the π* states present strong trigonal warping, as expected for Dirac cones. These states do not display a predominant spin character. In Figure 4(b,c), the non-dispersive Eu 4f band is visible around 1.49 eV binding energy and shows a predominant minority spin character. Interestingly, the flat π* band is characterized by a prevalence of the majority spin polarization, as clearly visible in the spin polarization plot on top of Figure 4(d), in line with the dedicated DFT calculations performed for this system [28].

These findings demonstrate the relevance of using Eu for efficiently tuning the Gr electronic properties and driving the interlayer magnetic coupling, opening new perspectives for its application in spintronic devices.

In conclusion, the integration of spin- and momentum-resolved photoemission spectroscopy into a PEEM-type instrument represents a significant advancement in the study of electronic structures of materials. In recent years, spin-resolved momentum microscopy has thus evolved into a very efficient tool for investigating electronic structures in detail, be it for magnetic and nonmagnetic crystals, 2D transition metal dichalcogenides, layered systems, or molecular hybrid systems. The ability to collect dense data sets across the entire Brillouin zone using the spin-resolved momentum microscopy setup installed at the NanoESCA beamline at Elettra offers deeper insights into band structure, exchange interactions, and spin-orbit effects of materials than have been available before. The wide range of photon energies, the choice of light polarization, and finally the time structure of the synchrotron radiation offer unique experimental opportunities for such an instrument. ■

References

1. P. S. Farago, *Rep. Prog. Phys.* **34** (3), 1055 (1971). doi:10.1088/0034-4885/34/3/305
2. R. Feder, *Polarized Electrons in Surface Physics* (World Scientific Publishing, 1985).
3. G. Bihlmayer et al., *Nat. Rev. Phys.* **4** (10), 642 (2022). doi:10.1038/s42254-022-00490-y
4. Y. Xu et al., editors. *Handbook of Spintronics* (Springer Science+Business Media, Dordrecht, 2016).
5. E. Bauer, *Surface Microscopy with Low-Energy Electrons* (Springer-Verlag, New York, 2014).
6. B. Krömker et al., *Rev. Sci. Instrum.* **79** (5), 053702 (2008). doi:10.1063/1.2918133
7. C. Tusche et al., *Ultramicroscopy.* **159**, 520 (2015). doi:10.1016/j.ultramic.2015.03.020
8. C. M. Schneider et al., *J. Electron Spectrosc. Relat. Phenom.* **185**, 330 (2012).
9. S. Schönhense et al., *Rev. Sci. Instrum.* **91** (12), 123110 (2020). doi:10.1063/5.0024074
10. S. Matsui et al., *Jpn. J. Appl. Phys.* **59** (6), 067001 (2020). doi:10.35848/1347-4065/ab9184
11. S. Ponzoni et al., *Adv. Phys. Res.* **2**, 2200016 (2023).
12. K. Medjanik et al., *Nat. Mater.* **16** (6), 615 (2017). doi:10.1038/nmat4875
13. D. Cocco et al., *Proc. SPIE.* **3767**, 271 (1999).
14. A. Locatelli et al., *J. Phys. IV.* **104**, 99 (2003).
15. K. Hagiwara et al., *arXiv:2205.15252.* (2022).
16. A. Polyakov et al., *Nat. Commun.* **13** (1), 2472 (2022). doi:10.1038/s41467-022-30093-1
17. P. M. Sheverdyaeva et al., *Phys. Rev. B.* **106**, 045108 (2022).
18. C. Tusche et al., *Appl. Phys. Lett.* **99**, 032505 (2011).
19. C. Tusche et al., *Ultramicroscopy.* **130**, 70 (2013). doi:10.1016/j.ultramic.2013.02.022
20. C. Tusche et al., *Nat. Commun.* **9** (1), 3727 (2018). doi:10.1038/s41467-018-05960-5
21. E. Młyńczak et al., *Phys. Rev. B.* **103**, 035134 (2021).
22. D. Janas et al., *Adv. Mater.* **35**, 2205698 (2023).
23. L. Plucinski et al., *Phys. Rev. B.* **80**, 184430 (2009).
24. B. Hammer et al., *Nature.* **376** (6537), 238 (1995). doi:10.1038/376238a0
25. S. Bhattacharjee et al., *Sci. Rep.* **6**, 35916 (2016). doi:10.1038/srep35916
26. M. Jugovac et al., *Carbon.* **198**, 188 (2022). doi:10.1016/j.carbon.2022.07.011
27. M. Jugovac et al., *Adv. Electron. Mater.* **9**, 2300031 (2023).
28. M. Jugovac et al., *Adv. Mater.* **35**, 2301441 (2023).